J. Mol. Biol. (1975) 97, 163–172

Structure of Tomato Bushy Stunt Virus

II.† Comparison of Results Obtained by Electron Microscopy and X-ray Diffraction

A. Jack‡, S. C. Harrison

Gibbs Laboratory, Harvard University
12 Oxford Street, Cambridge, Mass. 02138, U.S.A.

and R. A. Crowther

Medical Research Council Laboratory of Molecular Biology
Hills Road, Cambridge CB2 2QH, England

(Received 8 January 1975)

A three-dimensional reconstruction from electron micrographs of tomato bushy stunt virus has been used to determine X-ray phases to 28 Å resolution, by analogy with the single isomorphous replacement method of protein crystallography. An electron density map computed from X-ray amplitudes and these phases differs in two important respects from the electron micrograph reconstruction. The exclusion of stain from the 5-fold vertices, previously attributed to the presence of a minor protein, is shown to be an artifact of staining. The other difference involves positive staining of the RNA at the quasi-3-fold positions.

1. Introduction

Electron microscopy and X-ray diffraction are complementary methods for studying macromolecular assemblies. The relative experimental advantages and disadvantages of the two methods are well known (see, e.g. Finch & Holmes, 1967). The technique of negative staining has proved particularly powerful for investigating structure to a resolution of about 25 Å. This domain is of great interest since it corresponds to the envelope dimensions of protein subunits. It is an especially difficult one for X-ray diffraction, which has been most useful in detecting larger periodicities (e.g. the helical parameters of muscle filaments) and in exploring atomic detail (e.g. protein structure).

In this paper we compare images of tomato bushy stunt virus revealed by negative staining and X-ray diffraction, and from the results attempt to answer two questions: (1) how faithful to the native, hydrated structure are details of the stain-embedded object? (2) Is the image obtained by electron microscopy adequate for determining phases of X-ray reflexions out to 25 Å resolution? The two questions are obviously not independent.

† Paper I in this series is Harrison, 1969.

‡ Present address: Medical Research Council Laboratory of Molecular Biology, Hills Road, Cambridge CB2 2QH, England.

Since we embarked on this work, Unwin (1974) has made a systematic study of this first question, using the stacked disc aggregate of tobacco mosaic virus protein. As a standard for comparison, he uses a three-dimensional reconstruction of the stacked disc (Unwin & Klug, 1974) from pictures taken using an electrostatic phase plate (Unwin, 1972), in which the contrast is due mainly to protein rather than stain. An equivalent reconstruction from images of negatively-stained particles using conventional electron microscopy but with very low electron exposures gave similar results, but as the exposure was increased, the images (and therefore the reconstructions) changed in a reproducible way, which Unwin explains in terms of shrinkage and movement of the stain. Optical diffraction patterns of the phase plate images are very similar to X-ray diffraction patterns of oriented sols of the stacked disc structure (Finch & Klug, 1974), indicating that the negatively stained and "native" structures are not grossly different. Unfortunately there is no X-ray structure to compare directly with the reconstructions.

In the case of TBSV†, X-ray crystallographic data and an electron density map are already available (Harrison, 1971; Harrison & Jack, 1975). For the comparison with electron microscopy, the crystals have one crucially important property: they are stable and have the same unit cell dimension in a variety of solvents of very different electron density (Harrison, 1969). If we can obtain Fourier maps of the virus in two such solvents, the difference between them will reveal the impenetrable regions of the virus particle. This is essentially the information yielded by electron microscopy using negative staining.

Previous workers (Longley, 1967; DeRosier & Oliver, 1971) have compared X-ray diffraction patterns with optical diffraction patterns obtained from electron micrographs of thin crystalline sections and two-dimensional arrays. Although such comparisons have provided useful structural information, they are only applicable at very low resolution. In contrast, a comparison of the electron microscope image with a *difference* electron density is quite rigorous, and from such a comparison we may hope to answer the two questions above.

2. Materials and Methods

(a) *Electron microscopy*

The reconstruction of a 3-dimensional image of TBSV from electron micrographs has been described previously (Crowther & Amos, 1971). The mathematical methods used have also been given in some detail (Crowther *et al.*, 1970).

(b) *X-ray data collection*

Three-dimensional data sets were collected on 3° precession photographs by the scheme described in the following paper (Harrison & Jack, 1975). For the present work, we used data corresponding to solvent electron densities of 0·351 (0·8 M-$(NH_4)_2SO_4$), 0·368 (1 M-Na_2SO_4) and 0·408 (4 M-$(NH_4)_2SO_4$) e/Å^3 (data sets 1, 2 and 3, respectively). As shown previously (Harrison, 1969), the solvent-dependent intensity changes are the same for sodium and ammonium sulphate and for sucrose, indicating that the intensity differences are caused solely by a solvent-exclusion effect.

† Abbreviations used: TBSV, tomato bushy stunt virus; SIR, single isomorphous replacement; F_{lo}, structure amplitude from low-salt crystal; F_{hi}, structure amplitude from high-salt crystal; MIR, multiple isomorphous replacement.

Of the 1322 independent reflexions at 16 Å resolution, 1072 could in principle be recorded by the precession strategy used. Most of the non-recorded reflexions were near the resolution limit, and thus not important for the comparison with electron micrographs. About 35% of the observable reflexions were too weak to give a measurable intensity in the exposure time used. It therefore became important to assign an appropriate sub-threshold amplitude ($F_{\min}$) to all such reflexions, in order to avoid artificially large differences between amplitudes just above and just below the threshold of observation. Data sets corresponding to different solvent densities were placed on a common scale by comparing reflexions between $|\mathbf{h}| = 20$ and $|\mathbf{h}| = 24$ which are relatively independent of solvent density.

(c) *Computational outline*

The computations fall into four parts, each of which will be described in detail later.

(i) *Parameter solution*

The parameters of the reconstructed electron microscope image were varied so as to maximize the agreement between structure amplitudes calculated from the image and the observed salt-dependent X-ray intensity changes.

(ii) *Phase determination*

Structure factors computed from the electron microscope image were used to determine phases for the X-ray amplitudes, by a method analogous to that of single isomorphous replacement.

(iii) *Phase refinement*

Methods based on non-crystallographic symmetry were used to improve the phases obtained in (ii), and to estimate phases which were not well-determined by the SIR method.

(iv) *Comparisons*

Various electron density maps and sets of phases determined from the electron microscope image were compared with those determined independently by X-ray methods alone.

3. Results

(a) *Parameter solution*

The reconstructed electron microscope image was stored as an array, $\rho(x,y,z)$, representing densities on an arbitrary scale, sampled at equal intervals (d) along x, y and z. The ideal negatively-stained particle is best represented by a three-dimensional step function which is zero outside the envelope defined by penetration of the stain and unity within it. In computing structure factors, $\mathbf{f}_{\text{calc}}$, from the reconstruction we therefore assigned unit weight to all points of the array for which $\rho(x,y,z)$ was greater than some minimum value ($\rho_{\min}$) and ignored all other points. Points lying farther than 170 Å from the centre of the particle were also ignored (although all values in this region were in any case less than $\rho_{\min}$), as were points at radii less than 130 Å. The latter exclusion, which improved structure amplitude agreement slightly, was prompted by two considerations: (1) the possible unreliability of uranyl acetate penetration at inner radii (there might indeed be some *positive* staining of RNA in this region), and (2) the difficulty of choosing an appropriate $\rho_{\min}$ for a large radial range, arising from the somewhat arbitrary treatment of the spherically-symmetric term in the reconstruction.

The two critical parameters for comparing computed structure amplitudes, $\mathbf{f}_{calc}$, with observed salt differences, ΔF, are thus the sampling interval d (equivalent to determining the linear scale of the reconstruction) and the minimum density, ρ_{min}. The two are not completely independent, since the computed structure factors depend primarily on the outer envelope. A small increase in d can be compensated by a small increase in ρ_{min} without significant change in the shape of the outer surface of the particle image. Amplitudes were scaled by comparing the sum of electron micrograph structure amplitudes with the sum of X-ray amplitude differences in shells of increasing resolution, in order to determine relative scale and temperature factors. Scale factors were computed using the centric reflexions, since only for these is the observed salt difference, ΔF, strictly equal to the vector difference between low and high salt amplitudes (see Fig. 1). Agreement was measured by the conventional R factor:

$$R = \frac{\sum||\mathbf{f}_{calc}| - |\Delta F||}{\sum|\Delta F|}.$$

Terms with $|\Delta F| < F_{min}$ were ignored in this comparison. Systematic variation of d and ρ_{min} showed a clear minimum in the R factor. We restricted the calculation to the resolution range between 50 Å and 28 Å, corresponding to $8 \leq |\mathbf{h}| \leq 14$. For lower orders the spherically symmetric component is significant; beyond 28 Å most of the observed salt differences and calculated structure factors are too small for meaningful comparison. The best combination of ρ_{min} and d gave $R = 0{\cdot}57$. For the best value of ρ_{min}, variation of d by more than 3% from its optimum increased R to more than 0·65. Comparison of computed structure factors with salt differences from data sets 1 and 3, and from 2 and 3, yielded essentially identical results.

(b) *Phase determination*

The crystal structure factor may be considered in two parts, one arising from the external shape of the particle and the other from internal density fluctuations. The salt differences depend only on the shape contribution, which is ideally that part

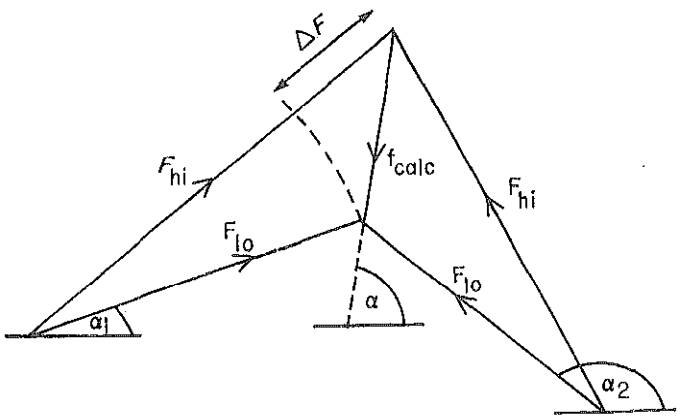

FIG. 1. SIR phase diagram interpreted for salt differences. The structure factors computed from the electron micrograph reconstruction give the salt difference vector $\mathbf{f}_{calc} = \boldsymbol{F}_{lo} - \boldsymbol{F}_{hi}$ in modulus and phase. The observed salt differences give $\Delta F = \big|\,|F_{lo}| - |F_{hi}|\,\big|$. α_1, α_2 are the two possible phases for $\boldsymbol{F}_{lo}$, and α the centroid phase.

revealed by negative staining. We may therefore regard the reconstruction as a "heavy atom" and use the structure factors calculated from it to determine X-ray phases by a method exactly analogous to the single isomorphous replacement method of protein crystallography (see, e.g. North & Phillips, 1969) (Fig. 1).

Structure factors ($\mathbf{f}_{calc}$) computed from the reconstructed image, using the best values of d and ρ_{min}, were used to determine centroid phases for X-ray reflexions with $8 \leq |\mathbf{h}| \leq 14$. Poorly determined phases were eliminated by neglecting terms for which: (1) $|\mathbf{f}_{calc}| > F_{lo} + F_{hl}$, since comparison of X-ray amplitudes for the three different salt densities showed that such "crossovers" were very few; (2) $\mathbf{f}_{calc} < 0{\cdot}5\ \Delta F$ or $\mathbf{f}_{calc} > 2\ \Delta F$. The three X-ray data sets permitted two independent phase calculations for each reflexion. Phases were computed using data sets 1,3 and 2,3 respectively, and accepted only if the two indications for data set 3 agreed to within 60°. Of the 173 observed reflexions with $8 \leq |\mathbf{h}| \leq 14$ in data set 2 (1 M-Na_2SO_4), phases for 64 were determined by this method. To this set were added the 25 non-zero terms with $|\mathbf{h}| \leq 6$, where the spherically symmetric component dominates and determines the sign (Harrison, 1971). The phases so determined will be referred to as the EM-SIR set. The equatorial section of a 28 Å Fourier map computed with these unrefined EM-SIR phases is shown in Plate I(a). The expected features of the surface are clearly present: the morphological units on the strict and quasi-2-fold axes and the secondary clustering about low density regions on the 5- and 3-fold (quasi-6-fold) axes (cf. below). The nature of this secondary clustering is not at all clear in the reconstructed electron microscope image, which suggests instead a rather broad hole on the quasi-6-fold axis and extra density on the 5-fold axis. We have thus obtained additional structural information by phasing the TBSV X-ray amplitudes from electron micrographs, even before including the constraint of icosahedral symmetry.

(c) *Phase refinement*

We improved and extended the phases for data set 2 (low salt) by icosahedral averaging, both in real space by rotation of the Fourier map, and in reciprocal space by using the symmetrizing H matrix (Crowther, 1969).

The matrix H was computed using the formulae given by Main & Rossman (1966) and Crowther (1967), counting as significant any interaction between two reflexions separated by five or fewer reciprocal lattice translations. Approximately 150 terms were retained from each row of the 432×216 matrix, the remainder being considered insignificantly small. A further variable parameter is the particle radius, which for TBSV is known to be about 165 Å. Previous experience with the H-matrix method has shown that the best results are obtained if the radius is somewhat overestimated (Jack, 1973). Trial calculations showed that a radius of 200 Å gave the lowest refinement residual, and this value was used subsequently.

The H matrix was applied iteratively to all reflexions with $0 \leq |\mathbf{h}| \leq 14$, starting from EM-SIR phases where available, and from random phases for the remaining reflexions. The process converged well, and was stopped after five cycles. The equatorial section of the resulting Fourier map (H-matrix phases combined with all observed amplitudes out to $|\mathbf{h}| = 14$) is shown in Plate I(b). The major surface features are now more sharply defined. The morphological units on the strict 2-fold axes have a distinctly flatter outline than those on the quasi-2-fold axes, these latter

having become somewhat pinched. The map also shows cavities on the 5- and quasi-6-fold axes. An attempt to extend the phases to $|\mathbf{h}| = 16$ by using a larger H matrix and starting with random phases between $14 \leq |\mathbf{h}| \leq 16$ was unsuccessful. The map showed clearly spurious detail and a general degradation of the surface features. The 5-fold redundancy of information implied by icosahedral symmetry does not appear sufficient for successful phase extension of this kind.

Direct icosahedral averaging is in principle equivalent to the H-matrix iterations (Bricogne, 1974), but differs in detail (there is no need, for example, to supply initially unphased reflexions with random phases). The results of one cycle of icosahedral averaging are shown in Plate I(c) and (d). Plate I(c) is simply the result of averaging the map from which Plate I(a) is taken; Plate I(d) uses phases computed from the averaged map, together with observed amplitudes. Both are similar to Plate I(b). The additional terms included in the map of Plate I(d) (phases calculated from the map of Plate I(c) combined with previously unphased amplitudes) appear to increase the contrast both of surface and internal features: the high density regions are better defined, and correspond in many respects to the high-density regions of the MIR X-ray map (Plate II(b)) (Harrison & Jack, 1975).

Table 1 summarizes a comparison of various phase sets with the best phases determined from X-ray data alone. Both methods of icosahedral averaging improve the agreement between electron microscope- and X-ray-determined phases, and both yield essentially the same result. We conclude that non-crystallographic symmetry is indeed useful in the course of a low-resolution structure determination, and that in the case of TBSV, reciprocal- and real-space methods have proved equally reliable.

(d) *Comparisons*

The computations outlined in the preceding section provide one measure of the agreement between the stain-embedded object and the native structure. But it is difficult to define a suitable objective agreement index in reciprocal space—e.g. an amplitude R factor or a mean phase agreement—since we cannot readily assess the effect of errors in F_{lo} and F_{hi} on d or ρ_{min} or on the agreement index itself. We have, moreover, no independent estimate of errors in the three-dimensional reconstruction. We therefore chose to make the comparison by direct inspection of models and of various Fourier maps.

Several comparisons are possible. We have relied primarily on the outer envelope of the best MIR Fourier map calculated both at "low" (28 Å) and "high" (16 Å) resolution, as a measure of the native structure (see Plate II(b)). We can also compare the reconstructed electron microscope image (Plate II(c)) with a solvent-density difference map (Plate II(d)), which corresponds to ammonium sulphate negative staining in the crystal. A suitable difference map requires two independent phase determinations. Our data presently include one derivative each at high (data set 3, methyl mercury nitrate derivative) and at low (data set 2, $PtCl_6^{=}$ derivative) solvent density. Phases for each have been determined by an SIR calculation followed by non-crystallographic symmetry refinement (Harrison & Jack, 1975) as in the EM-SIR procedure described above. We have computed a solvent-difference map with coefficients equal to the vector differences between high- and low-salt structure factors (Plate II(d)). This map should show only the surface features which are masked out

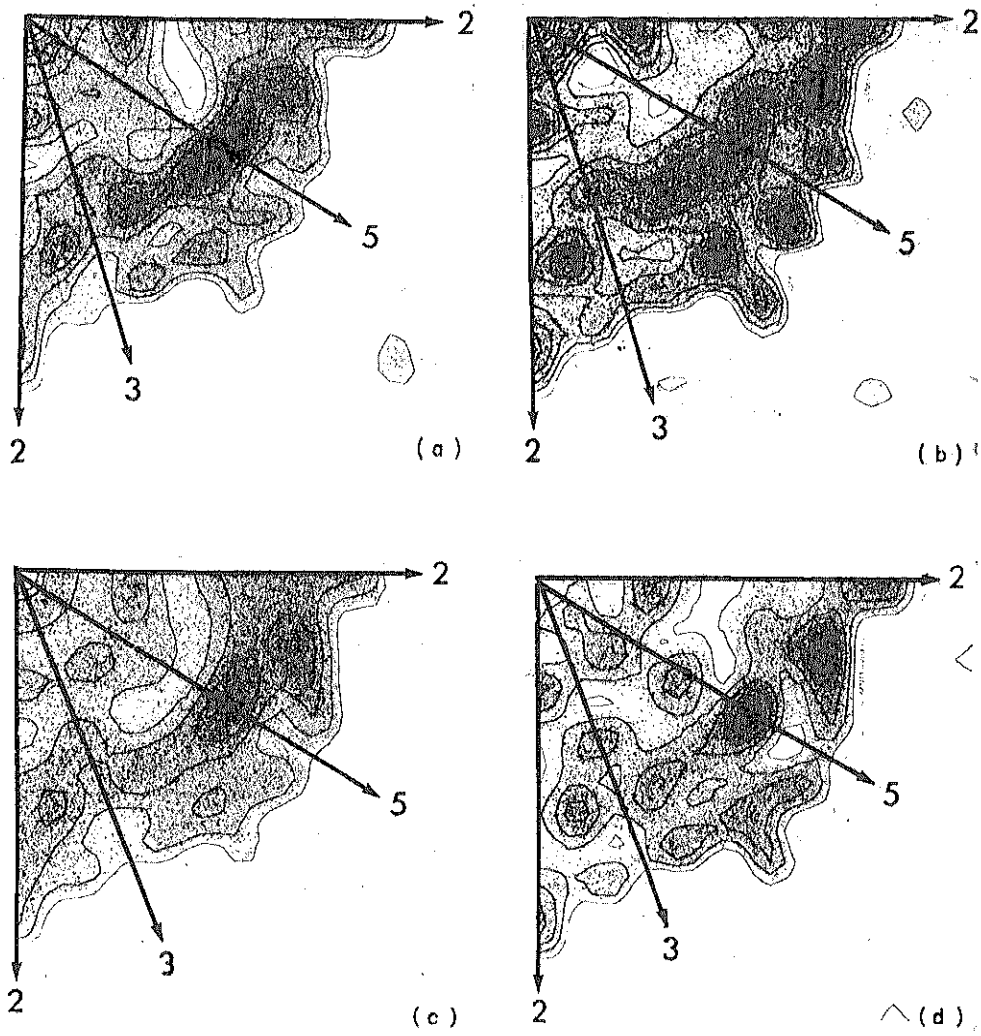

PLATE I. Equatorial sections of 28 Å electron density maps, phased from the electron micrograph reconstruction.

(a) EM-SIR map: X-ray amplitudes with phases directly from the electron micrograph reconstruction.

(b) H-matrix map: X-ray amplitudes with H-matrix refined phases.

(c) Direct space averaged map (icosahedral average of (a)).

(d) Direct space refined map: X-ray amplitudes with phases from (c).

[*facing p. 168*

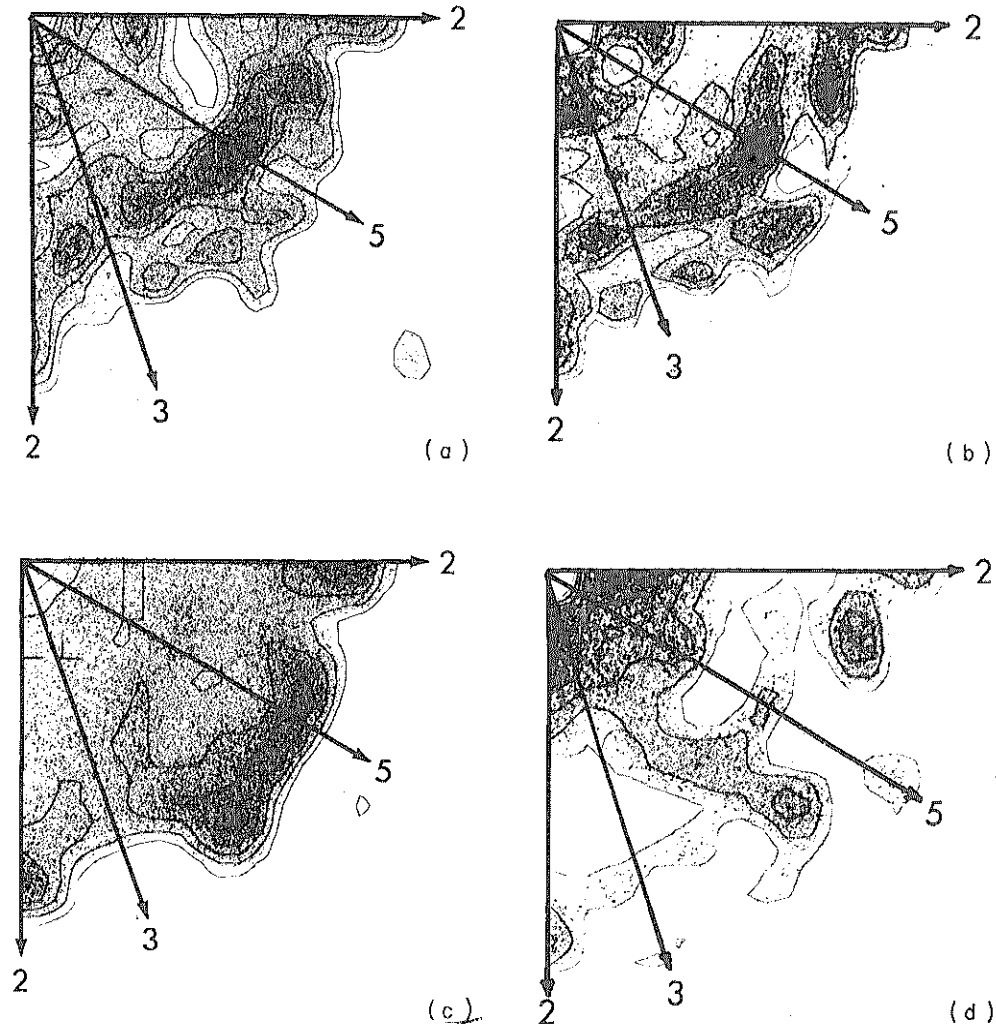

PLATE II. (a) 28 Å electron density map (X-ray amplitudes) phased only from the electron micrograph reconstruction. Same as Plate I(a).

(b) 28 Å electron density map phased by isomorphous replacement and non-crystallographic symmetry. This is our most reliable image of the "native" structure.

(c) Equatorial section of the electron micrograph reconstruction.

(d) Salt-difference Fourier map, computed using coefficients $|F'_{1o}| \exp(i\alpha_{1o}) - |F_{h1}| \exp(i\alpha_{h1})$, with phases α_{1o} as used for the map in Plate II(b), and phases α_{h1} computed as described in the text.

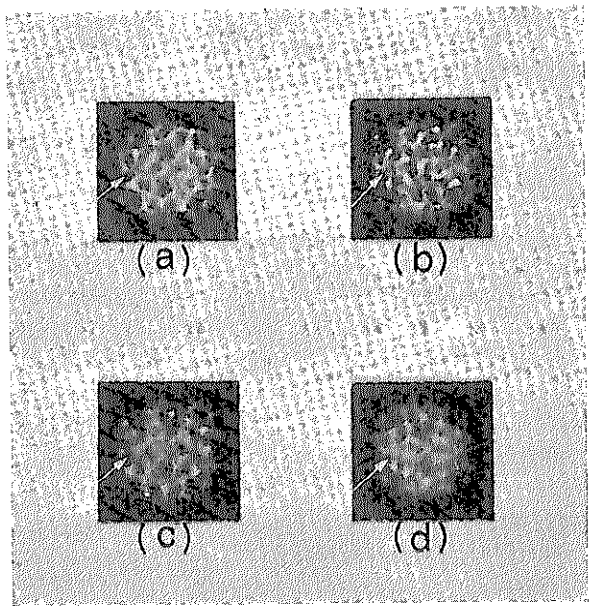

PLATE III. Electron micrographs of 2-fold views of TBSV negatively stained with uranyl acetate. Images (c) and (d) show stain exclusion around the 5-fold axes (arrowed); images (a) and (b) show stain penetration.

by high electron-density solvent (as in the reconstruction itself). The main features of the map are the expected projections on the 2-fold and quasi-2-fold axes. The high density at the centre of the particle is spurious, and arises from a few very low-order difference coefficients which are not well-determined.

We have also evaluated the refined EM-SIR phases in a way that is independent of the heavy-atom dependent MIR phases. Insofar as the relative strength of features in the electron microscope-phased map accurately represents the structure, we should be able to simulate an increase in solvent density by "filling in" all regions of the map with $\rho < \rho_{\min}$. We can then use the resulting density to compute structure factors for the high-salt data (data set 3). The parameter $\rho_{\min}$ is chosen to correspond to the particle envelope, and the density in the exterior space thereby defined is set to a level, ρ_o, representing the new solvent density. In practice, $\rho_{\min}$ and ρ_o can both be refined to give the best agreement between observed high-salt amplitudes and calculated structure factors from the filled-in low-salt map. We obtained $R = 0{\cdot}55$ (all terms with $6 \leq |\mathbf{h}| \leq 14$, $F > F_{\min}$), with the best ρ_o slightly greater than $\rho_{\min}$, as expected for data set 3 where the solvent density is just greater than the estimate for hydrated TBSV protein (Harrison, 1969). Small variation of ρ_o or $\rho_{\min}$ gave R values $> 0{\cdot}6$.

4. Discussion

(a) *How faithful to the native structure are details of the stain-embedded object?*

The principal features of the reconstructed electron microscope image (cf. Crowther & Amos, 1971) are concentrations of stain-excluding density on the strict and local 2-fold axes. These dimeric morphological units form rings of five about the 5-fold axes and rings of six about the 3-fold axes. Each dimer has the shape of an inverted V with its apex at the surface of the virus and its arms spreading inward toward the 5-fold and strict 3-fold axes (Fig. 2). These units define deep stain-filled pockets on the quasi-3-fold positions. The units on the local 2-fold axes, which lie at a radius some 10 Å greater than those on the strict 2-folds, have one arm extending toward a 5-fold axis and the other toward a 3-fold; the units on the strict 2-fold axes have one arm extending toward each of the neighbouring 3-fold axes. There is a considerably greater concentration of density on the 5-fold than on the 3-fold axes.

The outer contours of the X-ray Fourier maps (Plates I and II(b)) show many features identical to the image just described. There appear, however, to be two important regions of difference: (1) the 5-fold positions do not have extra density at an outer radius. The X-ray map shows that each subunit has an additional projecting side-arm (Fig. 2(c)) which, when repeated by the symmetry, forms a ring around the opening of an internal cavity on the 5-fold axis. No similar ring occurs about the quasi-6-fold axis because of the tilting of the dimers. The cavity on the 5-fold axis is accessible in the crystal to sulphate ion as shown by the solvent-density difference map (Plate II(d)). Moreover some images of negatively stained TBSV do show uranyl acetate penetration at these positions. The view down a 2-fold axis is particularly characteristic: representative particles are shown in Plate III. Stain exclusion from the 5-fold axis has been attributed by Crowther & Amos (1971) to a protein species of molecular weight 28,000 found as a minor component in TBSV preparations (Butler, 1970). Ziegler *et al.* (1974) have shown, however, that this component is a cleavage product of the coat protein and that it is present only in minute quantities in TBSV

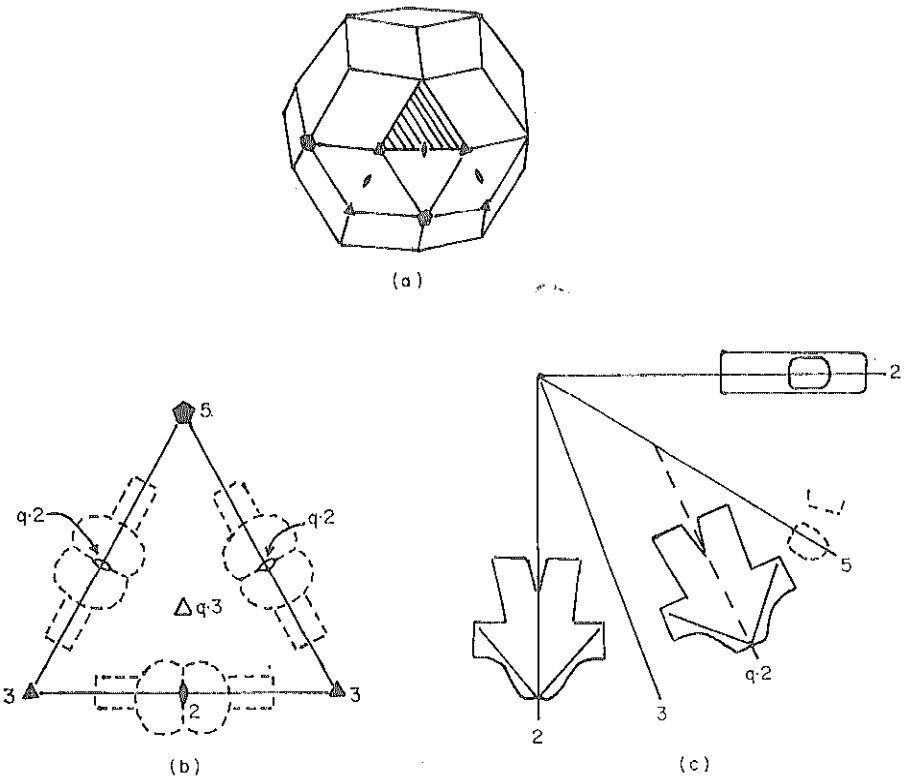

FIG. 2. Schematic representation of subunit arrangement in TBSV.

(a) Rhombic triacontahedron showing some of the icosahedral symmetry elements. This Figure is particularly suitable for representing the quasi-equivalent packing in TBSV, since the local 3-fold axis at the centre of each half-facet is parallel to the nearest strict 2-fold axis.

(b) Half-facet of triacontahedron showing disposition of subunits. Filled symbols represent strict symmetry axes, open symbols local axes. q.2, quasi-2-fold; q.3 quasi-3-fold.

(c) Equatorial section through virus particle, showing how the "side arms" produce the characteristic appearance around different symmetry axes. Dotted lines represent subunits which are not in the plane of the paper.

crystals. Gel electrophoresis of redissolved crystals indicates less than 0·3 chains of 28,000 molecular weight protein per virus particle and no other discrete species (except for the large chain, always present as a single copy per particle (cf. Ziegler *et al.*, 1974). Micrographs from redissolved crystals exhibit both types of image, showing that not all the 5-fold axes have been penetrated by negative stain. Variable entry of uranyl acetate into the 5-fold cavity therefore probably accounts for the variety of images obtained. The opening of this cavity has a diameter of only about 20 Å (Harrison & Jack, 1975). There may also be some shrinkage of the stain when exposed to the beam (Unwin, 1974), which tends to make the stain withdraw from the cavity. The images selected for the reconstruction presumably had relatively few stain-filled 5-fold axes.

(2) The pockets at quasi-3-fold position are less pronounced in the MIR Fourier and in EM-SIR phased maps than in the reconstructed electron microscope image. Moreover, the X-ray maps have a very high-density feature at these positions,

extending out to a radius of about 135 Å. This feature probably represents portions of the RNA chain near the quasi-3-fold axes. We suggest that the greater depth of the uranyl-acetate filled pocket at these positions (in the electron-micrograph reconstruction) may be caused by positive staining of the RNA.

It is clear that caution should be exercised in interpreting three-dimensional image reconstructions of stained nucleoprotein complexes. Not only may there be stain movements which tend to exaggerate certain features (Unwin, 1974), but also cavities which the stain does not penetrate or penetrates in a variable way. There may also be difficulties in deciding whether certain features should be ascribed to positive or negative staining.

(b) *Is the image obtained by electron microscopy adequate for determining phases of X-ray reflexions?*

A variety of criteria indicate that we have correctly determined phases of X-ray reflexions from the electron microscope image. Comparison with the independently determined MIR phases (Table 1) is the most objective index, but at this stage we cannot assess accurately different contributions to the mean phase angle differences.

TABLE 1

Mean deviations of various phase sets from refined X-ray phases

	EM-SIR	Calculated from averaged EM-SIR map	EM-SIR after H-matrix refinement
64 reflexions directly phased by electron microscopy	50°	38°	35°
All reflexions with $8 < h < 14$	—	43°	47°

EM-SIR, see Results, section (b).

We have been able to use the phases obtained from the reconstruction to help locate the heavy atoms in an isomorphous $PtCl_6^{2-}$ derivative of TBSV (Harrison & Jack, 1975). A difference Fourier map at 28 Å resolution showed three sites, two of which were known from previous work (Harrison, 1971). Doubtless we were helped in this case by the fact that the sites are less than 10 Å from 3- and 5-fold axes, so that the difference map shows a small number of very high peaks. We cannot be certain that the method would work for a derivative in which the heavy atoms were less clustered.

The appearance of the EM-SIR map is in some ways a more revealing criterion. The use of X-ray amplitudes with electron microscope-determined phases leads to a map similar to the three-dimensional reconstruction but altered in reasonable ways (e.g. the cavity on the 5-fold axis) and showing plausible internal detail. In cases where an independent MIR phase determination is not possible, such criteria will be the only ones available.

Several important limitations to the use of electron microscopy for solving the X-ray phase problem have become apparent in the course of our calculations. First,

it is clear that we obtained reasonable initial agreement between calculated and observed amplitudes only by using solvent-density *difference* amplitudes from the X-ray data. For particles with less marked internal density fluctuations (e.g. structures built only of protein) the distinction may be less critical, but with a nucleoprotein complex it is unlikely that we could have obtained a reasonable start by using the low-salt data alone. Second, we have been unable to extend the phase determination beyond a resolution of 28 Å ($|\mathbf{h}| > 14$), despite the use of non-crystallographic symmetry. This is certainly in large part a result of the limited resolution of the reconstructed electron microscope image, and the relatively fewer strong salt-difference terms at higher resolution. It may also be that differences between the stain-embedded object and the envelope of the native structure, noted in the preceding paragraph, became important enough at 28 Å resolution to affect the phase determination. Despite these limitations, use of electron microscope phases with X-ray amplitudes has certainly extended and clarified our view of the TBSV particle.

We are grateful to C. Schutt for critical discussion of the manuscript. This work was supported by Public Health Service Research grant CA-13202 to one of us (S. C. H.). Some of the electron microscopy was supported by Public Health Service grant GM-06637 (to the E.M. Service Lab of the Biological Laboratories, Harvard University). Another author (A. J.) acknowledges the award of a fellowship from the Jane Coffin Childs Memorial Fund for Medical Research.

REFERENCES

Bricogne, G. (1974). *Acta Crystallogr. sect. A*, **30**, 395–405.
Butler, P. J. G. (1970). *J. Mol. Biol.* **52**, 589–593.
Crowther, R. A. (1967). *Acta Crystallogr.* **22**, 758–764.
Crowther, R. A. (1969). *Acta Crystallogr. sect B*, **25**, 2571–2580.
Crowther, R. A. & Amos, L. A. (1971). *Cold Spring Harbor Symp. Quant. Biol.* **36**, 489–494.
Crowther, R. A., DeRosier, D. J. & Klug, A. (1970). *Proc. Roy. Soc. ser. A*, **317**, 319–340.
DeRosier, D. J. & Oliver, R. M. (1971). *Cold Spring Harbor Symp. Quant. Biol.* **36**, 199–203.
Finch, J. T. & Holmes, K. C. (1967). In *Methods in Virology* (Maramorosch, K. & Koprowski, H., eds), vol. 3, pp. 351–474. Academic Press, New York.
Finch, J. T. & Klug, A. (1974). *J. Mol. Biol.* **87**, 633–640.
Harrison, S. C. (1969). *J. Mol. Biol.* **42**, 457–483.
Harrison, S. C. (1971). *Cold Spring Harbor Symp. Quant. Biol.* **36**, 495–501.
Harrison, S. C. & Jack, A. (1975). *J. Mol. Biol.* **97**, 173–191.
Jack, A. (1973). *Acta Crystallogr. sect. A*, **29**, 545–554.
Longley, W. (1967). *J. Mol. Biol.* **30**, 323–327.
Main, P. & Rossmann, M. G. (1966). *Acta Crystallogr.* **21**, 67–72.
North, A. C. T. & Phillips, D. C. (1969). In *Progress in Biophysics and Molecular Biology* (Butler, J. A. V. & Noble, D., eds), vol. 19, pp. 5–132. Pergamon Press, Oxford,
Unwin, P. N. T. (1972). *Proc. Roy. Soc. ser. A*, **329**, 327–359.
Unwin, P. N. T. & Klug, A. (1974). *J. Mol. Biol.* **87**, 641–656.
Unwin, P. N. T. (1974). *J. Mol. Biol.* **87**, 657–670.
Ziegler, A., Harrison, S. C. & Leberman, R. (1974). *Virology*, **59**, 509–515.